A novel distance protection scheme using time-frequency analysis and pattern recognition approach

P.K. Dash [a,*], S.R. Samantaray [b]

[a] *Centre for Research in Electrical, Electronics and Computer Engineering, Bhubaneswar, Orissa, India*
[b] *National Institute of Technology, Rourkela, India*

Abstract

This paper presents a new approach for distance protection of transmission lines using time-frequency analysis. The proposed technique consists of preprocessing the fault current signal samples using hyperbolic S-transform to yield the change in energy and standard deviation at the appropriate window variation. From these two features, a decision of fault or no-fault on any phase or multiple phases of the transmission line can be made. The ground detection is done by a proposed indicator with a threshold value. The fault distance from the relaying point can be accurately estimated using cubic polynomial interpolation technique, Feed forward Neural Network and Adaptive Network Fuzzy Inference System (ANFIS).

Keywords: ANFIS; Change energy; Cubic interpolation; Distance protection; HS-transform; Neural network; Standard deviation

1. Introduction

Transmission line protection is a very important issue to safeguard the electric power system. The faults on transmission lines need to be detected, classified, located accurately, and cleared as fast as possible. In power transmission line protection, faulty phase identification and location of fault from the relaying point are the two most important issues, need to be addressed. Distance relaying techniques based on the measurement of the impedance at the fundamental frequency between the fault location and the relaying point have attracted wide spread attention. The sampled voltage and current data at the relying point are used to locate and classify the fault involving the line with different fault resistance present in the fault path.

The accuracy of the fault classification and location also depends on the amplitude of the DC offset and harmonics in comparison to the fundamental component. Fourier Transforms, Differential equations, Waveform modeling and Kalman filters are some of the techniques used for fault detection and location calculation. Another pattern recognition technique based on wavelet transform [1] has been found to be an effective tool in monitoring and analyzing power system disturbances including power quality assessment and system protection against faults. Although wavelets provide a variable window for low and high frequency currents in the current waveforms during fault, they are subject to inaccuracies due to noise and the presence of harmonics.

Here in this paper, a new approach for fault classification and location using multi resolution S-transform with windows of varying shape [4] is proposed. The S-transform [2–7] is an invertible time-frequency spectral localization technique that combines elements of wavelet transforms and short-time Fourier transform. The S-transform uses an analysis window whose width is decreasing with frequency providing a frequency dependent resolution. S-transform is continuous wavelet transform with a phase correction. It produces a constant relative bandwidth

* Corresponding author. Tel.: +91 9437003306.
E-mail address: pkdash_india@yahoo.com (P.K. Dash).

analysis like wavelets while it maintains a direct link with Fourier spectrum. The S-transform has an advantage in that it provides multi resolution analysis while retaining the absolute phase of each frequency. This has led to its application for detection and interpretation of events in a time series like the power quality disturbances [6].

A variant of the original S-transform is used where a pseudo-gaussian hyperbolic window is used to provide better time and frequency resolutions at low and high frequencies instead of the S-transform using the Gaussian window for fault classification and location in transmission lines. Here the hyperbolic window has frequency dependence in its shape in addition to its width and height. The increased asymmetry of the window at low frequencies leads to an increase in the width in the frequency domain, with consequent interference between major noise frequencies. In this paper the hyperbolic S-transform (HS-transform) is used to calculate the change in energy and standard deviation of the fault current signal to identify the fault classes and hence obtain the fault distance from the relaying point. The voltage signal samples are not taken in this approach as it gives the same feature as current signal, which only increases computational burden.

The simulation is done using PS Blockset of Simulink (MATLAB). The transmission line model is developed to generate fault data with different system operating conditions. The interpolation algorithm, Feed Forward Neural Network and ANFIS are used to compute the fault distance from the relaying point, with error less than 0.5–1% in most cases.

2. HS-transform for fault pattern recognition

The S-transform is an extension to the Gabor Transform and wavelet transform, and is based on a moving and scalable localizing Gaussian window. The interesting phenomena in the S-transform is that it is fully convertible both forward and inverse from time domain to frequency domain. This properties is due to the fact that the modulating sinusoids are fixed with respect to the time axis while the localizing scalable Gaussian window dilates and translates. The S-transform falls within the broad range of multi-resolution spectral analysis, where the standard deviation is an inverse function of the frequency, thus reducing the dimension of the transform.

The localizing Gaussian window function $g(t)$ is defined as

$$g(t) = \frac{1}{\sigma\sqrt{2\pi}} \exp^{-\left[\frac{t^2 f^2}{2\sigma^2}\right]} \tag{1}$$

where σ is the standard deviation. The multiresolution S-transform can be defined as

$$S(f,\tau,\sigma) = \int_{-\infty}^{\infty} h(t) g(\tau - t, \sigma) \exp^{-i2\pi 2\pi} \mathrm{d}t \tag{2}$$

The primary purpose of the dilation parameter is to increase the width of the window function $g(t,\sigma)$ for lower frequency and vice versa, and is controlled by selecting a specific functional dependency of σ with the frequency. The width of the window is chosen to be proportional to the period of the cosinusoid being localized.

$$\sigma(f) = T = \frac{1}{|f|} \tag{3}$$

where T is the time period.

Now the S-transform [4] may be written as

$$S(\tau,f) = \int_{-\infty}^{\infty} h(t) \left\{ \frac{|f|}{\sqrt{2\pi}} \exp\left\{-f^2(\tau - t)/2\right\} \exp(-2\pi f t) \right\} \mathrm{d}t, \tag{4}$$

where S denotes the S-transform of $h(t)$, which is the actual fault current or voltage signal varying with time, frequency is denoted by f, and the quantity τ is a parameter which controls the position of gaussian window on the time-axis.

Here a small modification of the gaussian window has been suggested for better performance.

$$W_{\mathrm{gs}}(\tau - t, f, \alpha_{\mathrm{gs}}) = \frac{|f|}{\sqrt{2\pi\alpha_{\mathrm{gs}}}} \exp \frac{[-f^2(\tau - t)]}{2\alpha_{\mathrm{gs}}^2} \tag{5}$$

and the S-transform with this window is given by

$$S(\tau, f, \alpha_{\mathrm{gs}}) = \int_{-\infty}^{\infty} h(t) \omega(\tau - t, f, \alpha_{\mathrm{gs}}) \cdot \exp(-2\pi \mathrm{i} f t) \mathrm{d}t, \tag{6}$$

where α_{gs} is to be chosen for providing suitable time and frequency resolution.

In applications, which require simultaneous identification time-frequency signatures of different faulted phase currents and voltages, it may be advantageous to use a window having frequency dependent asymmetry. Thus, at high frequencies where the window is narrowed and time resolution is good, a more symmetrical window needs to be chosen. On the other hand, at low frequencies where a window is wider and frequency resolution is less critical, a more asymmetrical window may be used to prevent the event from appearing too far ahead on the S-transform. Thus an hyperbolic window of the form given below is used.

$$W_{\mathrm{hy}} = \frac{2|f|}{\sqrt{2\pi(\alpha_{\mathrm{hy}} + \beta_{\mathrm{hy}})}} . \exp\left\{\frac{-f^2 X^2}{2}\right\} \tag{7}$$

Where

$$X = \frac{\alpha_{\mathrm{hy}} + \beta_{\mathrm{hy}}}{2\alpha_{\mathrm{hy}}\beta_{\mathrm{hy}}}(\tau - t - \xi) + \frac{\alpha_{\mathrm{hy}} - \beta_{\mathrm{hy}}}{2\alpha_{\mathrm{hy}}\beta_{\mathrm{hy}}} \times \sqrt{(\tau - t - \xi)^2 + \lambda_{\mathrm{hy}}^2} \tag{8}$$

In the above expression $0 \langle \alpha_{\mathrm{hy}} \langle \beta_{\mathrm{hy}}$ and ξ is defined as

$$\xi = \frac{\sqrt{(\beta_{\mathrm{hy}} - \alpha_{\mathrm{hy}})^2 \lambda_{\mathrm{hy}}^2}}{4\alpha_{\mathrm{hy}}\beta_{\mathrm{hy}}} \tag{9}$$

The translation by ξ ensures that the peak W_{hy} occurs at $\tau - t = 0$.

At $f = 0, W_{hy}$ is very asymmetrical, but when f increases, the shape of W_{hy} converges towards that of W_{gs}, the symmetrical gaussian window given in Eq. (4) for different values of α_{hy} and β_{hy} and with $\lambda_{hy}^2 = 1$. The discrete version of the Hyperbolic S-transform of the faulted current signal samples at the relaying point is calculated as $S[n,j] = \sum_{m=0}^{N-1} H[m+n] \cdot G(m,n) \exp(i2\pi mj)$ where N is the total number of samples and the indices n, m, j are $n = 0,1 \ldots N-1, m = 0,1 \ldots ..N-1,$ and $j = 0,1 \ldots N-1$. The $G(m,n)$ denotes the Fourier transform of the Hyperbolic window and is given by

$$G(m,n) = \frac{2|f|}{\sqrt{2\pi(\alpha_{hy} + \beta_{hy})}} \exp\left(\frac{-f^2X^2}{2n^2}\right) \quad (10)$$

and

$$X = \frac{(\alpha_{hy} + \beta_{hy})}{2\alpha_{hy}\beta_{hy}} t + \frac{\beta_{hy} - \alpha_{hy}}{2\alpha_{hy}\beta_{hy}} (\sqrt{t^2 + \lambda_{hy}}) \quad (11)$$

and $H(m,n)$ is the frequency shifted discrete Fourier transform $H[m]$, where

$$H(m) = \frac{1}{N} \sum_{m=0}^{N-1} h(k) \exp(-i2\pi nk) \quad (12)$$

3. System studied

The 400 kV, 3-phase, 100 km power transmission line is shown in Fig. 1. A cycle-to-cycle comparison of currents and thresholds are used to detect any abnormality due to the occurrence of a fault. Once a deviation is observed, the HS-transform is applied to the data one cycle back and the one cycle data from the point of occurrence of the deviation in the current amplitudes. The parameters of the transmission line chosen as $R = 0.2568\ \Omega$/km, $L = 2.0$ mH/km, $C = 0.0086\ \mu$F/km. The Fig. 2 shows the current signal at LLL–G fault. The sampling rate for the simulation is 6.4 kHz.

Here, the fault pattern recognition is done by HS-transform for L–G, LL–G, and L–L, LLL–G faults with fault resistance ranging from 0 Ω to 200 Ω at various location and inception angles. The standard deviation and change in energy are the two indices found out for faulty phase detection and location determination.

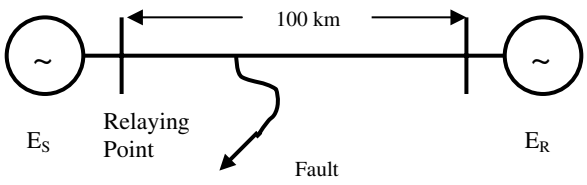

Fig. 1. Transmission line model.

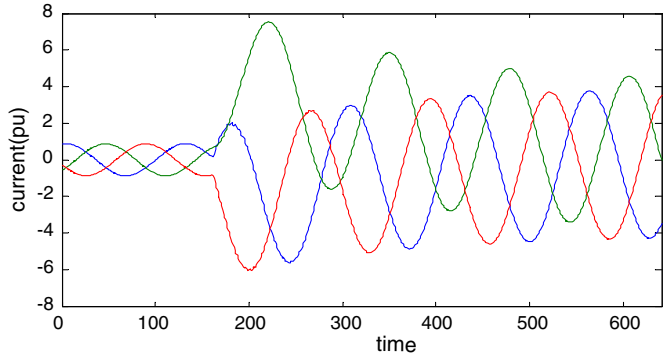

Fig. 2. Fault current at LLL–G fault.

4. Faulty phase identification

The feature extracted from the faulted current signal using HS-transform for different types of faults at 5–95% of the line are used to classify the type of fault. Change in the signal energy is obtained as $ce = E_f - E_A = \{abs(hs_f\}^2 - \{abs(hs_n\}^2$ and the standard deviation of the HS-transform contour is obtained as $sd = std\ \{abs(hs_f)\}$.

Various types of faults are simulated on the system shown in Fig. 1 with varying inception angle, distance and fault resistance R_f in the fault path to ground. Figs. 3a–3n shows the time frequency contours of the HS-transform output for a–g (a-phase and ground), a–b (between a- and b-phase), a–b–g (a and b to ground) and a–b–c–g (a-, b-, c-phase to ground) faults. From these figures, it is seen that the faulted phase exhibits the distinct contours and the time at which it occurs. The phase, which is not faulted, exhibits no such contours, thus clearly classifying the type of fault visually. For recognizing the fault pattern, the change in energy of the signal (ce) and standard deviation (sd) are used and the detailed results for different types of fault inception angles, distance and fault resistance.

Tables 1–6 show the change energy (ce) and standard deviation (sd) for all the three phases in faulted condition. It is clearly seen that, in case of L–G(a–g) fault at 10% of

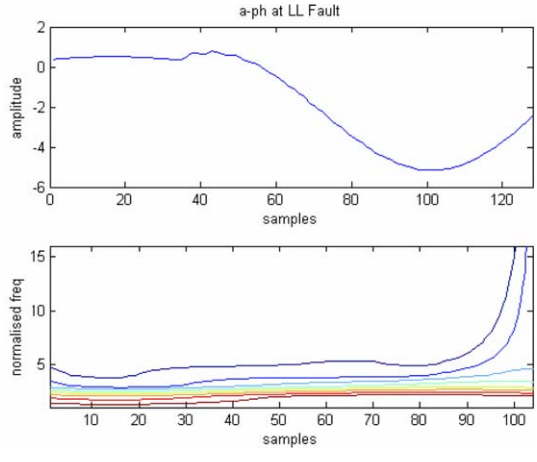

Fig. 3a. a-ph at LL fault at 10% of line, R_f 20 Ω.

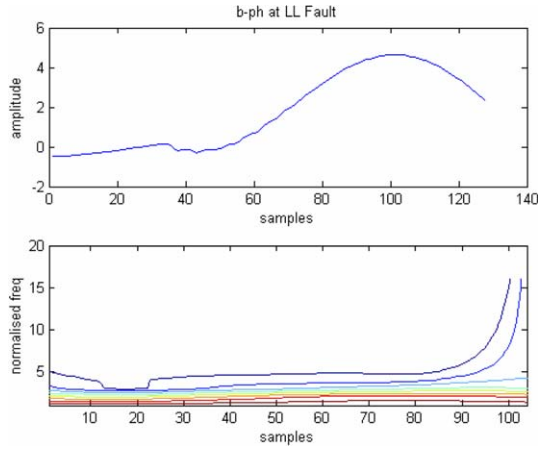

Fig. 3b. b–ph at LL fault at 10% of line, R_f 20 Ω.

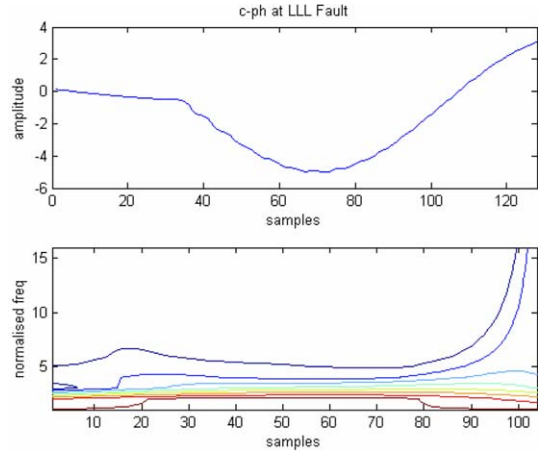

Fig. 3c. c–ph at LLL fault at 30% of line, R_f 100 Ω.

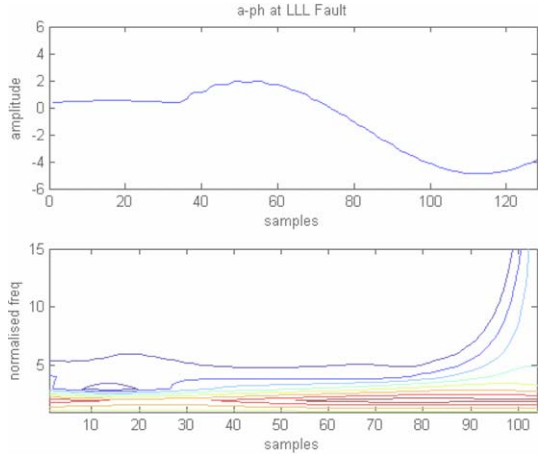

Fig. 3d. a-ph at LLL fault at 30% of line, R_f 100 Ω.

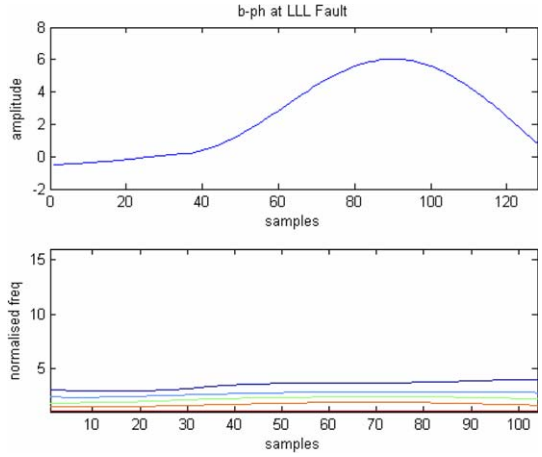

Fig. 3e. b–ph at LLL fault at 30% of line, R_f 100 Ω.

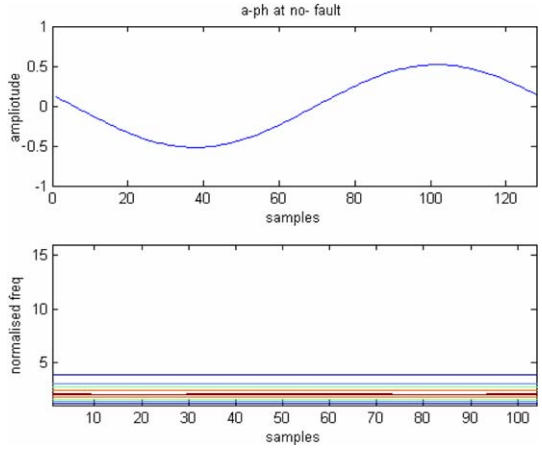

Fig. 3f. a-ph at no-fault.

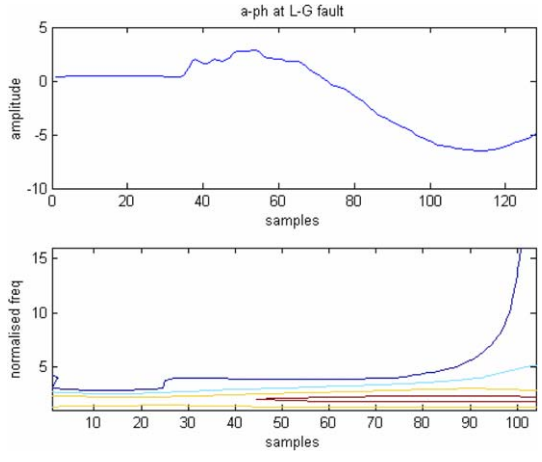

Fig. 3g. a-ph at L–G fault at 50% of line, R_f 150 Ω.

line, 20 Ω fault resistance and 30° inception angle, the ce and sd value for a-phase are 49.6137 and 0.6269 respectively, while for phase b , ce and sd are 3.3263 and 0.0698 and for c-phase ce and sd are 1.0416 and 0.0481 respectively. The value of ce and sd in a-phase clearly shows that there is fault in a-phase. Likewise in case of LL–G (ab–g) fault, ce and sd for a-phase are 49.7764 and 0.6724 respectively. For b-phase ce and sd are 18.90 and

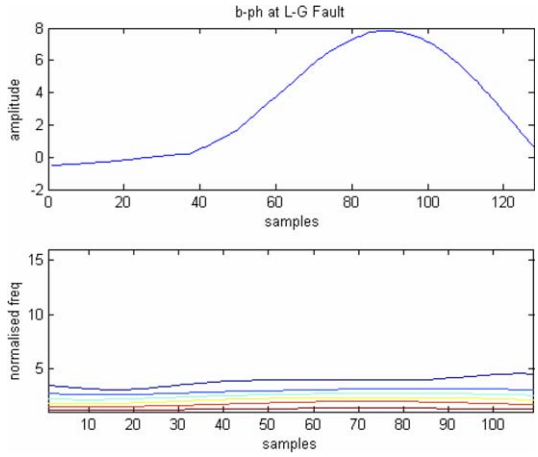

Fig. 3h. b–ph at L–G fault at 50% of line, R_f 150 Ω.

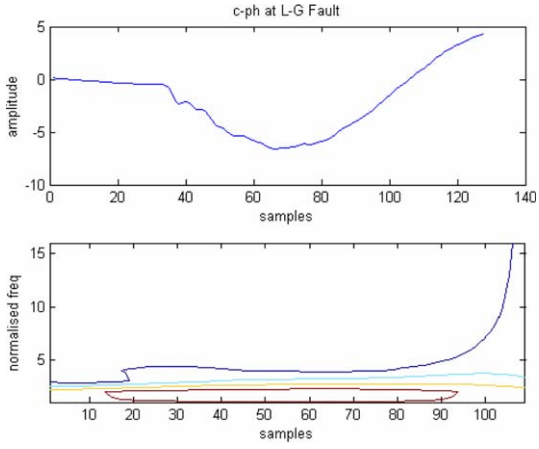

Fig. 3i. c–ph at L–G fault at 50% of line, R_f 150 Ω.

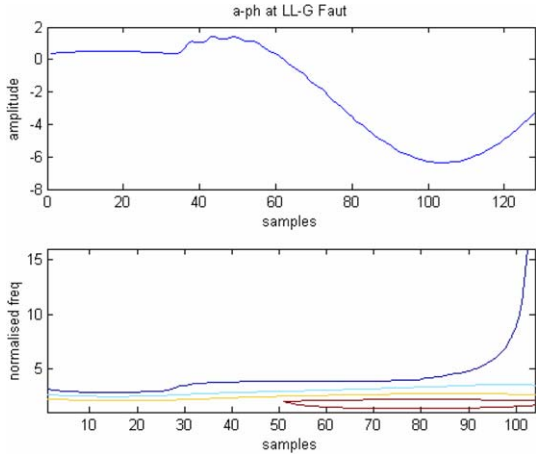

Fig. 3j. a-ph at LL–G fault at 70% of line, R_f 200 Ω.

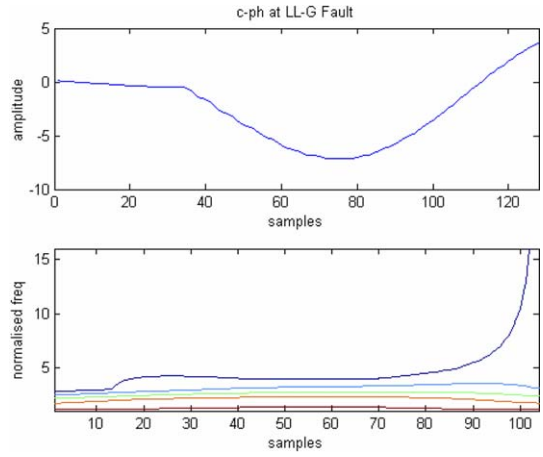

Fig. 3k. c–ph at LL–G fault at 70% of line, R_f 200 Ω.

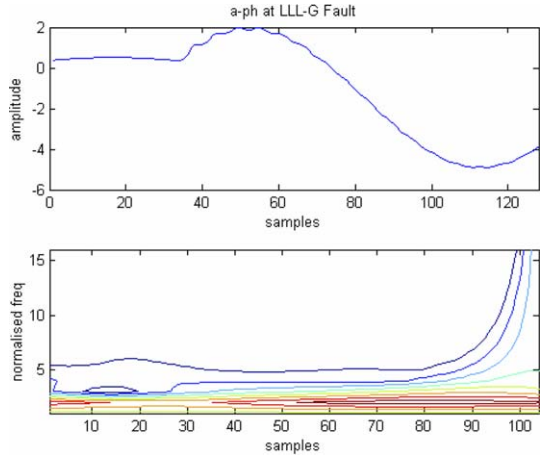

Fig. 3l. a-ph at LLL–G fault at 90% of line, R_f 200 Ω.

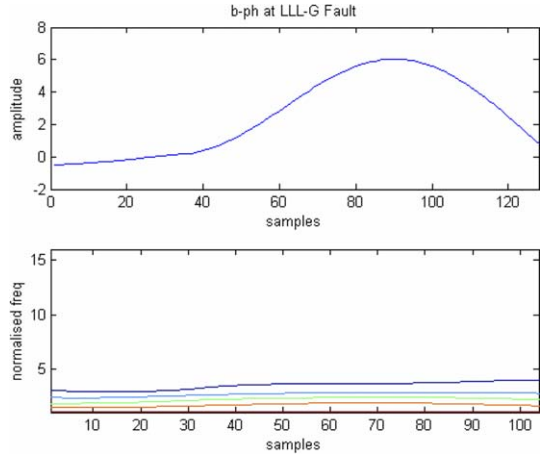

Fig. 3m. b–ph at LLL–G fault at 90% of line, R_f 200 Ω.

0.29, respectively and for c-phase ce and sd are 2.01 and 0.06 respectively. The above result clearly shows that the phase involving fault is having very high value of ce and sd compared to un-faulted phase. Table 4 provides ce andsd for fault at 50% location, 200 Ω fault resistance and 90° inception angles. In case of L–L (ab) fault, ce and sd values for a-phase are 8.8929 and 0.1422, respectively and for b-phase, ce and sd are 7.7138 and 0.1231 while for c-phase ce and sd are 0.0000 and 0.0350 respec-

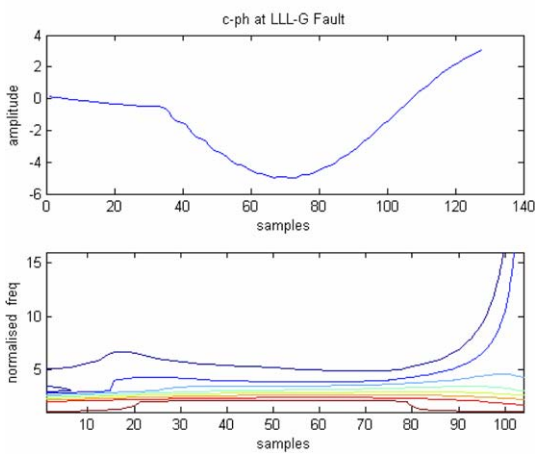

Fig. 3n. c–ph at LLL–G fault at 90% of line, R_f 200 Ω.

tively. For above location and fault resistance, for LLL–G(abc–g), ce and sd values for a-phase are 12.7833 and 0.1799, ce and sd values for b-phase are 8.132 and 0.1327 and ce and sd values for c-phase are 11.5229 and 0.1965 respectively, which indicates that all three phases are in faulted condition. The ce and sd values for different phases at different fault resistance, fault inception angle, fault location and for different types of fault have been shown in Tables 1–6. From the above analysis fault classification can easily done to detect the faulty phase. A general rule can be formulated for change in energy (ce) > 5.0 and standard deviation (sd) > 0.1 for the phase involving fault otherwise the phase is un-faulted.

5. Ground detection

Ground detection is done by a simple approach by defining an indicator.

$$\text{Indicator} = \min(\text{ce}_a, \text{ce}_b, \text{ce}_c)$$

In case of L–L (ab) fault at 10% of line with fault resistance of 20 Ω and 30° inception angle, the indicator is 0.0001. But the indicator is 1.0416 in case of L–G(a–g) fault, 2.0117 in case of LL–G(ab–g), and 16.2684 in case of LLL–G(abc–g) fault respectively. When the threshold value for indicator is more than 0.005, the fault involves ground, otherwise fault does not involve ground. This is verified for every kind of fault at different location, fault resistance and inception angles.

6. Fault location

Once the fault is classified, the next item is to determine the exact distance of the fault from the relaying point. For this purpose it is proposed to compute the ce and sd values for faults at different locations with varying inception angles, pre-fault load current values, and different fault resistances R_f in the fault path.

Here we propose three methods for fault location calculation and a comparative study has been made to get the accuracy of fault location.

Here the error is calculated as

$$\%\ \text{error} = \frac{|\text{actual distance} - \text{calculated distance}|}{\text{protected line length}} \times 100 \tag{13}$$

6.1. Method 1: Cubic Interpolation

In the first approach, polynomial curve fitting (cubic) has been applied. Here a relationship between fault distance d and ce can be expressed as

$$d = a_0 + a_1(\text{ce}) + a_2(\text{ce})^2 + a_3(\text{ce})^3 \tag{14}$$

In a similar way another relationship between d and sd is obtained as

$$d = a_0 + a_1(\text{sd}) + a_2(\text{sd})^2 + a_3(\text{sd})^3 \tag{15}$$

Here the polynomial of third order has been selected to fit the data covering the total distance and a wide range of fault resistance R_f and inception angle δ. Table 7 gives the actual distance calculation using the cubic interpolation technique. The maximum error is 0.06% in case of LL–G fault at 40% of transmission line.

6.2. Method 2: Feed Forward Neural Network

In the second approach a feed forward neural network with an input layer, two hidden layers, and an output layer is trained using back-propagation algorithm. The first hidden layer has five neurons and uses the tan-sigmoid function as the transfer function and the second hidden layer uses a pure linear sigmoid function for its activation. The output layer has got one neuron and uses log-sigmoid activation function and provides the fault location as output. In the back propagation training algorithm, the error measure E is given as

$$E = \sum_{J=1}^{Q} (d_j - x_i)^2 \tag{16}$$

where Q is the number of training samples. The weights are updated as

$$\Delta w(k+1) = -\eta \Delta_w E + \alpha \Delta w(k) \tag{17}$$

where $\Delta_w E$ is the gradient with respect to w, and $\propto$ is the momentum constant and η is the learning rate. The gradient descent algorithm is implemented in patch mode and an adaptive learning rate is used to keep the step size as large as possible without oscillations. Both sd and ce values are generated for 500 test cases (for different line sections, fault resistance R_f and inception angle δ) for training. Once the net is trained, any new value of sd and ce will yield the fault distance. From the results presented in Table 7, it is seen that the maximum error in the evaluation of fault distance

Table 1
Faulty phase identification

$R_f = 20\ \Omega$, Fault at 10%, Inception angle 30°							
Fault		a		b		c	
		ce_a	sd_a	ce_b	sd_b	ce_c	sd_c
LG	ag	49.6137	0.6269	3.3263	0.0698	1.0416	0.0481
	bg	1.7655	0.0859	24.9729	0.3148	3.1497	0.0920
	cg	2.1833	0.0592	1.0604	0.0538	34.9404	0.5415
LLG	abg	49.7764	0.6724	18.9028	0.2907	2.0117	0.0610
	bcg	3.3505	0.0703	36.7778	0.4392	43.9432	0.6116
	cag	42.5899	0.5139	2.4216	0.0841	24.9239	0.4324
LL	ab	24.2053	0.3070	22.2882	0.2856	0.0001	0.0350
	bc	0.0001	0.0350	11.5396	0.2076	10.1772	0.2003
	ca	26.7541	0.3909	0.0001	0.0350	28.0509	0.4028
LLLG	abcg	33.7419	0.4424	16.2684	0.2178	23.1498	0.3767

Table 2
Faulty phase identification

$R_f = 200\ \Omega$, fault at 30%, Inception angle 45°							
Fault		a		b		c	
		ce_a	sd_a	ce_b	sd_b	ce_c	sd_c
LG	ag	15.8385	0.2117	0.2464	0.0396	0.0230	0.0378
	bg	0.9986	0.0647	11.2101	0.1739	1.1876	0.0647
	cg	0.4431	0.0475	0.2272	0.0442	14.9927	0.2370
LLG	abg	16.4559	0.2231	8. 9539	0.1491	0.1174	0.0415
	bcg	0.2905	0.0323	11.7237	0.1727	12.5895	0.1969
	cag	13.4441	0.1825	0.4681	0.0559	15.3726	0.2517
LL	ab	9.9518	0.1473	8.1618	0.1281	0.0000	0.0350
	bc	0.0000	0.0350	8.2121	0.1577	7.1622	0.1526
	ca	13.1622	0.1526	0.0001	0.0350	12.3702	0.1854
LLLG	abcg	13.4585	0.1874	8.5023	0.1370	12.1127	0.2046

Table 3
Faulty phase identification

$R_f = 0\ \Omega$, fault at 30%, inception angle 60°							
Fault		a		b		c	
		ce_a	sd_a	ce_b	sd_b	ce_c	sd_c
LG	ag	53.6753	0.6884	2.0811	0.0572	0.4064	0.0410
	bg	2.3987	0.0757	26.8833	0.3412	3.2008	0.0800
	cg	1.6748	0.0562	0.9305	0.0504	35.25	0.5514
LLG	abg	52.8872	0.7219	18.8112	0.2796	1.1625	0.0489
	bcg	1.7182	0.0512	41.0512	0.4916	48.2312	0.6806
	cag	48.2917	0.5965	2.2728	0.0718	22.5077	0.3926
LL	ab	26.6698	0.3360	24.7842	0.3158	0.0001	0.0350
	bc	0.0001	0.0350	11.2606	0.1976	9.8353	0.1896
	ca	28.7006	0.4210	0.0001	0.0350	29.9979	0.4328
LLLG	abcg	36.7997	0.4865	17.7464	0.2351	23.9085	0.3904

occurs for an LL–G fault at 100 km from the relaying point and its magnitude is 1.38%.

6.3. Method 3: Adaptive Network Fuzzy Inference System (ANFIS)

In the third method, an adaptive network fuzzy inference system is trained for 500 test sets of ce and sd for various locations of faults, fault resistance and fault inception angles. The ANFIS structure has two inputs ce and sd and each of these contains 5 membership functions and the total number of rules in the fuzzy rule base is 25. Further, the membership function chosen here is a bell shaped one and has the form:

$$\mu_{A_i}(x) = \frac{1}{1 + \left(\frac{x - c_i}{a_i}\right)^{b_i}} \tag{18}$$

Table 4
Faulty phase identification

$R_f = 200\ \Omega$, fault at 50%, inception angle 90°							
Fault		a		b		c	
		ce_a	sd_a	ce_b	sd_b	ce_c	sd_c
LG	ag	14.2844	0.1947	0.0551	0.0365	0.3697	0.0419
	bg	1.1669	0.0667	10.4977	0.1615	0.9766	0.0645
	cg	0.3176	0.0443	0.4479	0.0453	13.5935	0.2180
LLG	abg	15.0194	0.2062	8.2011	0.1365	0.116	0.0421
	bcg	0.116	0.0421	10.773	0.1639	11.2391	0.1818
	cag	12.3907	0.1708	0.5111	0.0583	14.4228	0.2366
LL	ab	8.8929	0.1422	7.7138	0.1231	0.0000	0.0350
	bc	0.0000	0.0350	7.862	0.1522	6.816	0.1471
	ca	10.5525	0.1664	0.0000	0.0350	11.7686	0.1781
LLLG	abcg	12.7833	0.1799	8.132	0.1327	11.5329	0.1965

Table 5
Faulty phase identification

$R_f = 200\ \Omega$, fault at 10%, inception angle 45°							
Fault		a		b		c	
		ce_a	sd_a	ce_b	sd_b	ce_c	sd_c
LG	ag	17.4713	0.2295	0.6927	0.0451	0.2538	0.0350
	bg	0.8430	0.0648	12.5204	0.1861	1.4074	0.0681
	cg	0.6854	0.0463	0.1306	0.0437	16.4686	0.2574
LLG	abg	18.0017	0.2406	9.7721	0.1632	0.1512	0.0405
	bcg	0.2849	0.0335	12.8119	0.1819	14.0022	0.2124
	cag	14.5258	0.1944	0.5134	0.0594	16.4302	0.2684
LL	ab	10.4262	0.1525	8.6269	0.1332	0.0001	0.0350
	bc	0.0001	0.0350	8.5845	0.1634	7.5322	0.1584
	ca	11.769	0.1811	0.0001	0.0350	12.992	0.1929
LLLG	abcg	14.1534	0.1952	8.8947	0.1413	12.719	0.2129

Table 6
Faulty phase identification

R_f=200 Ω, fault at 100%, inception angle 30°							
Fault		a		b		c	
		ce_a	sd_a	ce_b	sd_b	ce_c	sd_c
LG	ag	13.0008	0.1752	0.5925	0.0717	2.9957	0.0891
	bg	2.4032	0.0725	12.1988	0.1611	0.4849	0.0587
	cg	0.2494	0.0351	2.1859	0.0581	15.0271	0.2869
LLG	abg	14.7122	0.1912	9.0009	0.1296	1.7841	0.0532
	bcg	1.9142	0.0760	14.3503	0.1830	12.5379	0.1727
	cag	10.3315	0.1448	1.5882	0.0628	17.0525	0.2311
LL	ab	10.3064	0.1464	7.8023	0.1178	0.0003	0.0350
	bc	0.0002	0.0350	12.0526	0.1645	10.4153	0.1539
	ca	10.7793	0.1575	0.0002	0.0350	13.1282	0.1774
LLLG	abcg	12.4227	0.1658	11.4536	0.1561	14.7028	0.2014

where the parameters a_i,b_i, and c_i are the parameters in the 1st layer and are updated with a generic formula as

$$\Delta\alpha = -\eta \frac{\partial E}{\partial \alpha} \tag{19}$$

and the learning rate η is expressed as

$$\eta = \frac{k}{\sqrt{\sum_{\alpha} \left(\frac{\partial E}{\partial \alpha}\right)^2}} \tag{20}$$

Table 7
(Fault location determination)

Fault	Actual distance	Calculated distance (cubic interpolation)	% error	Calculated distance (feed forward neural network)	% error	Calculated distance (ANFIS)	% error
LG	20	20.0139	+0.0139	19.9984	−0.0016	19.9995	−0.0005
	40	39.9487	−0.0513	40.0066	+0.0066	40.0011	+0.0011
	60	59.9654	−0.0346	59.9872	−0.0128	59.9989	−0.0011
	80	79.9866	−0.0134	80.0120	+0.0120	80.0012	+0.0012
	100	100.0199	+0.0199	99.9957	−0.0043	99.9993	−0.0007
LLG	20	20.0092	+0.009	18.7054	−1.2946	20.0017	+0.0017
	40	39.9395	−0.0605	40.7390	+0.7390	39.9976	−0.0024
	60	59.9807	−0.0193	61.3410	+1.3410	60.0010	+0.0010
	80	80.0102	+0.010	80.5931	+0.5931	79.9992	−0.0008
	100	99.9672	−0.0328	98.6215	−1.3785	100.0005	+0.0005
LL	20	19.9846	−0.015	19.3712	−0.6288	20.0024	+0.0024
	40	39.9921	−0.007	40.3648	+0.3648	39.9925	−0.0075
	60	59.9846	−0.015	60.6153	+0.6153	60.0109	+0.0109
	80	79.9911	−0.008	80.2577	+0.2577	79.9917	−0.0083
	100	100.0273	+0.027	99.3911	−0.6089	100.0025	+0.0025
LLLG	20	19.9892	−0.0108	19.4889	−0.5111	20.0024	+0.0024
	40	39.9886	−0.0114	40.2876	+0.2876	39.9993	−0.0007
	60	59.9833	−0.0167	60.5061	+0.5061	60.0005	+0.0005
	80	79.9824	−0.0176	80.2142	+0.2142	79.9996	−0.0004
	100	100.0284	+0.0284	99.5032	−0.4968	100.0002	+0.0002

where k is the step size, representing the length of each gradient transition in the parameter space. The final output from the ANFIS is of the form:

$$d = a_0 + a_1(\text{ce}) + a_2(\text{ce})^2 + b_1(\text{sd}) + b_2(\text{sd})^2 \quad (21)$$

The second layer gives the output as a product of the membership values as the firing strengths of the rules in this layer and the third layer calculates the value

$$f_i = \frac{\mu_i}{\sum \mu_i} \quad (22)$$

The fourth layer computes the defuzzified values using centroid defuzzification technique and the output layer generates the fault distance. On comparison of above three methods for HS-Transform based location on transmission lines, the ANFIS method produces the least amount of computational error as seen from Table 7. However, cubic interpolation technique is found to be the simplest and does not have any computational overhead. On the contrary, the ANFIS yields the most accurate result regarding the fault distance, but the computational overhead is found to be large.

7. Conclusion

In this paper S-transform based time frequency analysis has been done to compute the standard deviation and change in energy at varying window. The change in energy (ce) and standard deviation (sd) provides a method to detect the faulty phases of the transmission line by a simple rule based approach based on certain threshold values. Once the faulty phases are identified, the fault distance can be computed by three different approaches as shown in this paper. The simplest amongst the three is the cubic interpolation technique, but the computationally intensive ANFIS method yields the most accurate result for fault location.

References

[1] Gauda M, Salama MA, Sultam MR, Chikhani AY. Power quality detection and classification using wavelet multi-resolution signal decomposition. IEEE Transn Power Delivery 1999;14:1469–76.

[2] Stockwell RG, Mansinha L, Lowe RP. Localization of complex spectrum: The S-transform. J Assoc Expl Geophys 1996;XVII(3):99–114.

[3] Mansinha L, Stockwell RG, Lowe RP. Pattern analysis with two dimensional spectral localization: Application of two dimensional S-transforms. Physica A 1997;239:286–95.

[4] Pinnegar CR, Mansinha Lalu. The S-transform with windows of arbitrary and varying window. Geophysics 2003;68:381–5.

[5] Livanos G, Ranganathan N, Jiang J. Heart sound analysis using the S-transform. IEEE Comp Cardiol 2000;27:587–90.

[6] Dash PK, Panigrahi BK, Panda G. Power quality analysis using S-transform. IEEE Power Delivery 2003;18:406–11.

[7] McFadden PD, Cook JG, Foster LM. Decomposition of gear vibration signals by the generalizes S-transform. Mech Syst Signal Proc 1999;13:691–707.